

# UC Santa Barbara

## UC Santa Barbara Previously Published Works

### Title

Patterned mechanical feedback establishes a global myosin gradient.

### Permalink

<https://escholarship.org/uc/item/6xp3h1p1>

### Journal

Nature Communications, 13(1)

### Authors

Gustafson, Hannah

Claussen, Nikolas

De Renzis, Stefano

et al.

### Publication Date

2022-11-17

### DOI

10.1038/s41467-022-34518-9

Peer reviewed

# Patterned mechanical feedback establishes a global myosin gradient

Received: 10 December 2021

Accepted: 27 October 2022

Published online: 17 November 2022

 Check for updates


Hannah J. Gustafson<sup>1,2</sup>, Nikolas Claussen<sup>1</sup>  , Stefano De Renzi<sup>3</sup>  & Sebastian J. Streichan<sup>1,2</sup>  

Morphogenesis, the coordinated execution of developmental programs that shape embryos, raises many fundamental questions at the interface between physics and biology. In particular, how the dynamics of active cytoskeletal processes are coordinated across the surface of entire embryos to generate global cell flows is poorly understood. Two distinct regulatory principles have been identified: genetic programs and dynamic response to mechanical stimuli. Despite progress, disentangling these two contributions remains challenging. Here, we combine *in toto* light sheet microscopy with genetic and optogenetic perturbations of tissue mechanics to examine theoretically predicted dynamic recruitment of non-muscle myosin II to cell junctions during *Drosophila* embryogenesis. We find dynamic recruitment has a long-range impact on global myosin configuration, and the rate of junction deformation sets the rate of myosin recruitment. Mathematical modeling and high frequency analysis reveal myosin fluctuations on junctions around a mean value set by mechanical feedback. Our model accounts for the early establishment of the global myosin pattern at 80% fidelity. Taken together our results indicate spatially modulated mechanical feedback as a key regulatory input in the establishment of long-range gradients of cytoskeletal configurations and global tissue flow patterns.

Active regulation of the cytoskeleton represents an important set of cell scale processes capable of driving morphogenesis in a variety of contexts<sup>1–3</sup>. Just as unbalanced forces in a tug of war lead to motion, tissue-scale gradients of subcellular localized cytoskeletal components create force imbalances that quantitatively predict tissue flows<sup>4–7</sup>. Understanding morphogenesis, then, requires a quantitative understanding of how such gradients are created. In some cases, relations between gene expression patterns establishing the body axis and the distribution of cytoskeletal components have been uncovered by molecular investigations<sup>8,9</sup>. For example, the anisotropic myosin distribution driving germband extension (GBE) in *Drosophila* depends on Toll family receptors downstream of pair-rule genes<sup>10</sup>. Although recent work suggests a link between Tolls and Rho activity upstream of

myosin, the quantitative picture of the molecular pathway that converts Toll patterns to anisotropic myosin localization remains incomplete<sup>2,11</sup>.

In addition to genetic inputs, growing evidence indicates that mechanical cues can influence the cell properties and behaviors that determine how a tissue deforms<sup>12–15</sup>, a class of phenomena we here refer to as “mechanical feedback”. While a feedback loop via Rho activation has been indicated in cell culture<sup>16,17</sup>, molecular analysis suggests that this mechanism might not be present in all organisms<sup>18</sup>. Other studies report local myosin recruitment in response to mechanical deformation, however, the molecular mechanism *in vivo* remains unknown<sup>12</sup>. Here, the role played by tissue-specific gene expression in controlling mechanical cues complicates the task of

<sup>1</sup>Department of Physics, University of California Santa Barbara, Santa Barbara, CA 93106, USA. <sup>2</sup>Biomolecular Science and Engineering, University of California Santa Barbara, Santa Barbara, CA 93106, USA. <sup>3</sup>EMBL Heidelberg, Meyerhofstrasse 1, 69117 Heidelberg, Germany.  e-mail: [nclaussen@ucsb.edu](mailto:nclaussen@ucsb.edu); [streicha@ucsb.edu](mailto:streicha@ucsb.edu)

disentangling the impact of a pure genetic deterministic program from the effects of dynamic, post-translational mechanical feedback mechanisms<sup>2</sup>. Furthermore, the mechanical coupling of cells affects how forces are transmitted across tissues<sup>19,20</sup> to activate putative mechano-sensitive processes<sup>21–23</sup>. Due to lack of tools for characterizing mechanics during organismal development<sup>24</sup>, it remains unclear what inputs cells sense, how far these effects reach, and what relevance they may have on morphogenetic outputs.

In this work, we take an integrated approach, combining quantitative investigation with theory and quantitative analysis. Noll et al.<sup>13</sup> developed a physical theory of tissue mechanics proposing “dynamic recruitment” of myosin as a mechanism to ensure the mechanical stability of a tension-dominated network. In its simplest form, dynamic recruitment predicts a specific quantitative signature, according to which rates of myosin are recruited proportional to rates of cell edge deformation. We test this hypothesis by combining light sheet microscopy<sup>25</sup>, optogenetics<sup>26</sup>, and quantitative analysis to characterize myosin-II dynamics on adherens junctions in response to the deformation of cell edges. As an experimental system, we focused on germband extension (GBE) during *Drosophila* gastrulation. GBE is characterized by the convergent extension of cells which leads to more than the twofold elongation of the body axis, and it involves cells immediately adjacent to the ventral furrow (VF)<sup>8</sup>. Immediately preceding, and indeed overlapping with, GBE is the process of VF formation, which represents a major source of tissue deformation driven by the collective contraction and invagination of approximately 1000 cells from the ventral surface of the embryo<sup>27</sup>. The remaining epithelial surface maintains mechanical integrity, such that cells outside of the VF become stretched to compensate for the greatly reduced number of cells spanning the same circumference<sup>27</sup>. These highly dynamic and overlapping processes result in substantial tissue flows that create potential for an interplay of morphogenetic processes. Indeed, previous works have suggested that VF formation<sup>21</sup> or posterior midgut invagination<sup>28</sup> could contribute to axis elongation during GBE. With our quantitative and global analysis, these contexts offer ideal opportunities to study the nature of dynamic recruitment as a possible mediator of such interactions during development.

To address this possibility, we first characterize the strain and myosin profiles in the wild-type embryo during VF formation and the fast phase of GBE. We next induce ectopic strain using optogenetically patterned contractility and measure the resulting changes to the previously measured myosin profile. Our initial findings from these perturbations suggested that the response may be patterned, prompting us to pursue a more detailed analysis of these experiments. We next asked whether this response could be observed at the single-cell scale, using high-resolution confocal microscopy to examine single junction dynamics, and developed a simple theoretical model to capture the observed dynamics. Finally, we show the developmental relevance of mechanical feedback by removing a major source of strain, the VF, and measuring the effect on the myosin profile and GBE. Our results demonstrate that cytoskeletal dynamics can be captured in a physical model that quantitatively accounts for the establishment of myosin-II patterns from strain rates and indicate that long-range gradients of cytoskeletal and tissue flow patterns are determined by spatially patterned mechanical feedback.

## Results

### Myosin rate and strain rate are correlated and graded along the DV axis

To quantitatively test whether cells measure edge deformation and proportionally recruit myosin (Fig. 1A), we use in toto-live imaging of fluorescently labeled non-muscle myosin-II (myosin) at subcellular resolution with confocal multi-view light sheet microscopy<sup>25,29</sup>. We first characterized the dynamics of myosin in wild-type embryos during VF formation and the fast phase of GBE by creating a standardized metric

to measure junctional myosin normalized to the cytoplasmic pool, which we refer to as the “junctional myosin accumulation” or JMA (see Supplementary Information “Single junction myosin accumulation measurements” for more detail). We specifically focus on the germband, the trunk region posterior to the cephalic furrow (CF), which is known to exhibit a characteristic pattern of anisotropic myosin that drives GBE<sup>29</sup>. Accordingly, we look exclusively at the junctional pool in this work because (i) it is by far the dominant pool in the germband during this time and (ii) previous work has shown that removing the medial pool does not affect myosin anisotropy of the junctional pool<sup>18</sup>. Furthermore, measuring myosin in this way allows for quantification of rates of changes in local density caused by myosin motors binding to the actin cortex at adherens junctions independent of the concentration of fluorescently marked motors. In a region of the germband close to the VF, myosin junctional accumulation increased significantly over the course of VF formation, specifically on junctions parallel to the dorsoventral (DV) axis (Fig. 1B). When this same measurement was applied to the entire surface of the embryo, a clear gradient with high myosin junctional accumulation adjacent to the VF and little to no junctional myosin on the dorsal region became evident (Fig. 1C). This gradient along the DV axis suggests that myosin dynamics vary by region. We thus divided the trunk into discrete regions along the DV axis and measured the myosin accumulation averaged within these regions as a function of time (Fig. 1D, E). Myosin accumulation in the region closest to the VF was initially low at the onset of VF formation and increased linearly during invagination, to then decrease after furrow internalization was completed (Fig. 1D). When analyzing myosin accumulation over time by region, we found that the rate of accumulation was spatially graded, steepening the gradient in myosin levels over the course of VF formation (Fig. 1E).

We next characterized the strain of cell edges during this time frame. Cells nearest the VF were stretched towards the ventral midline giving rise to an anisotropic cell shape oriented towards the VF (Fig. 1F). While this effect was first observed in cells immediately adjacent to the furrow, it rapidly spread across the DV axis as furrow formation progressed and eventually reached the dorsal pole leading to stretching of the dorsal cells as previously reported<sup>27</sup>, although this takes place outside of the time period examined here. Single-cell edge tracking revealed cell edges oriented parallel to the DV axis and adjacent to the VF were strongly strained (i.e. elongated) as VF forms (Supplementary Movie 1). This effect decreased systematically with increasing distance from the furrow (Fig. 1G). Therefore, both the rate of myosin recruitment (Fig. 1H) and the rate of strain (Fig. 1H') showed a clear trend, with the highest rates immediately dorsal to the VF and steadily decreasing along the DV axis. Plotting the myosin accumulation rate versus the strain rate revealed a strong correlation between the two (Fig. 1I). While the relation between genetic patterning and myosin anisotropy during GBE is well documented, it is currently unknown how a DV myosin gradient emerges on cell edges<sup>9,30</sup>. Our analysis demonstrates that the characteristic anisotropic myosin pattern of the germband occurs concomitantly with VF formation and that the germband begins to move as the DV myosin gradient steepens. These observations suggest that the strain generated by the VF plays a role in establishing the global myosin anisotropy pattern during GBE.

### Strain rate induces myosin recruitment

Testing whether a causal mechanism underlies the relation between strain and myosin recruitment rates requires non-invasive methods capable of modifying strain rates<sup>26,31</sup>. We turned to optogenetics to transiently activate the cytoskeleton in spatially restricted domains to induce cell contraction and monitored the resulting changes in cellular flow, strain, and myosin dynamics in adjacent regions. To this end, we transiently activated a Cry2-CIBN-based RhoGEF2 optogenetic module with a spatially patterned infrared beam from a femtosecond laser<sup>26</sup>. As

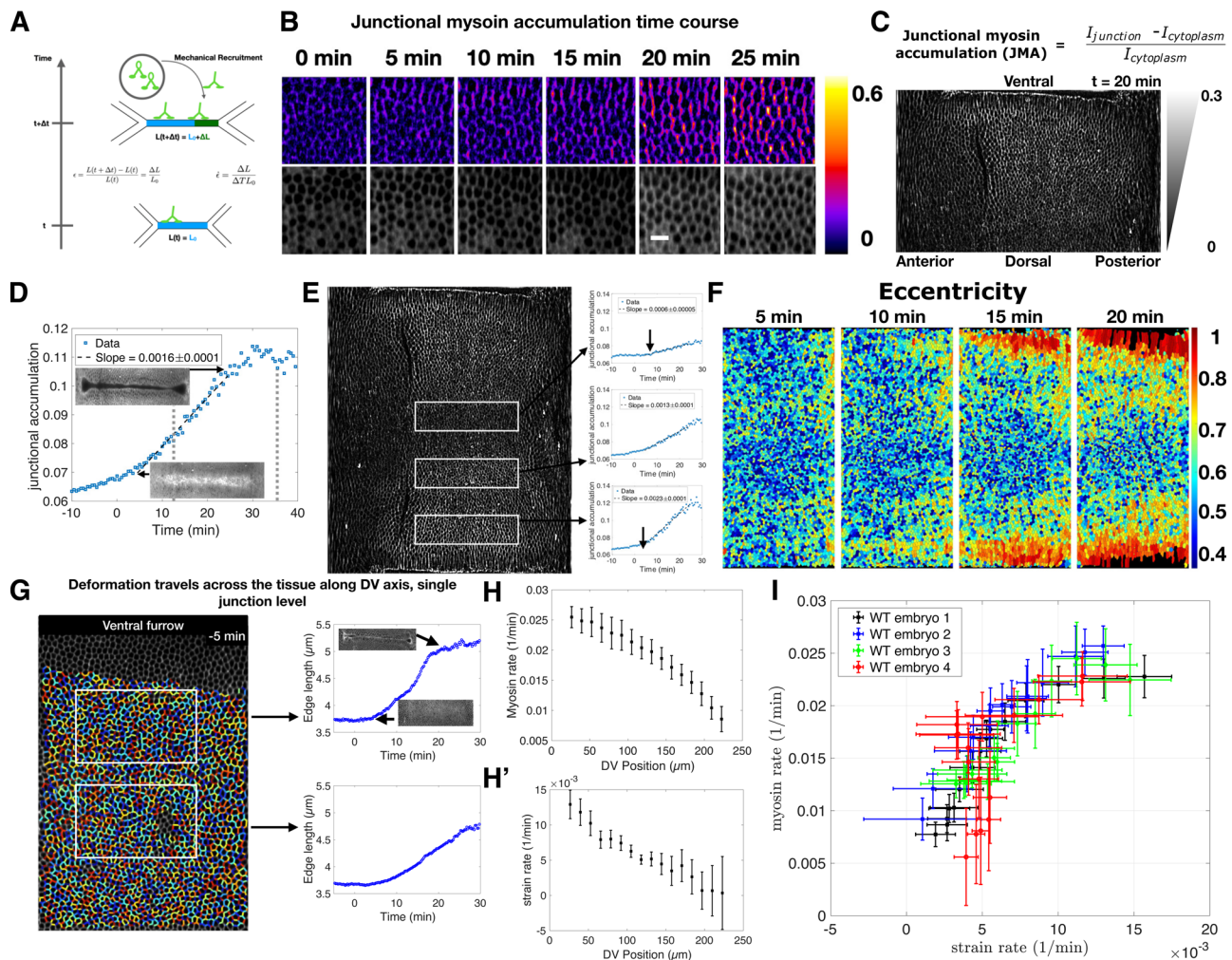


**Fig. 1 | Correlation between strain rate and myosin recruitment rate on individual junctions.** **A** Schematic representation of the proposed mechanical feedback mechanism. Equations define strain ( $\epsilon$ ) and strain rate ( $\dot{\epsilon}$ ) calculated from the percent change in cell edge length ( $\Delta L/L_0$ ) per time ( $\Delta T$ ). **B** Top: Junctional myosin accumulation (JMA, see **C**) over time in a region of the lateral ectoderm (Fig. S1J).  $t = 0$  corresponds to 10 min before the onset of ventral furrow (VF) formation. Bottom: sqh::mCherry signal 4  $\mu\text{m}$  below adherens junction. **C** JMA (defined at the top, see Supplementary Information) on one side of the embryo (Fig. S1J) during early germband elongation (20 min after VF initiates). Triangles represent JMA gradation along the DV axis. **D** JMA over time on cell edges located in a single region of the embryo (middle box in **E**). Typically a box contains  $n = 400$  edges. Insets show the VF in sqh::mCherry expressing embryo at the corresponding time point. Arrows designate a time period from -10 to 20 min post CF formation over

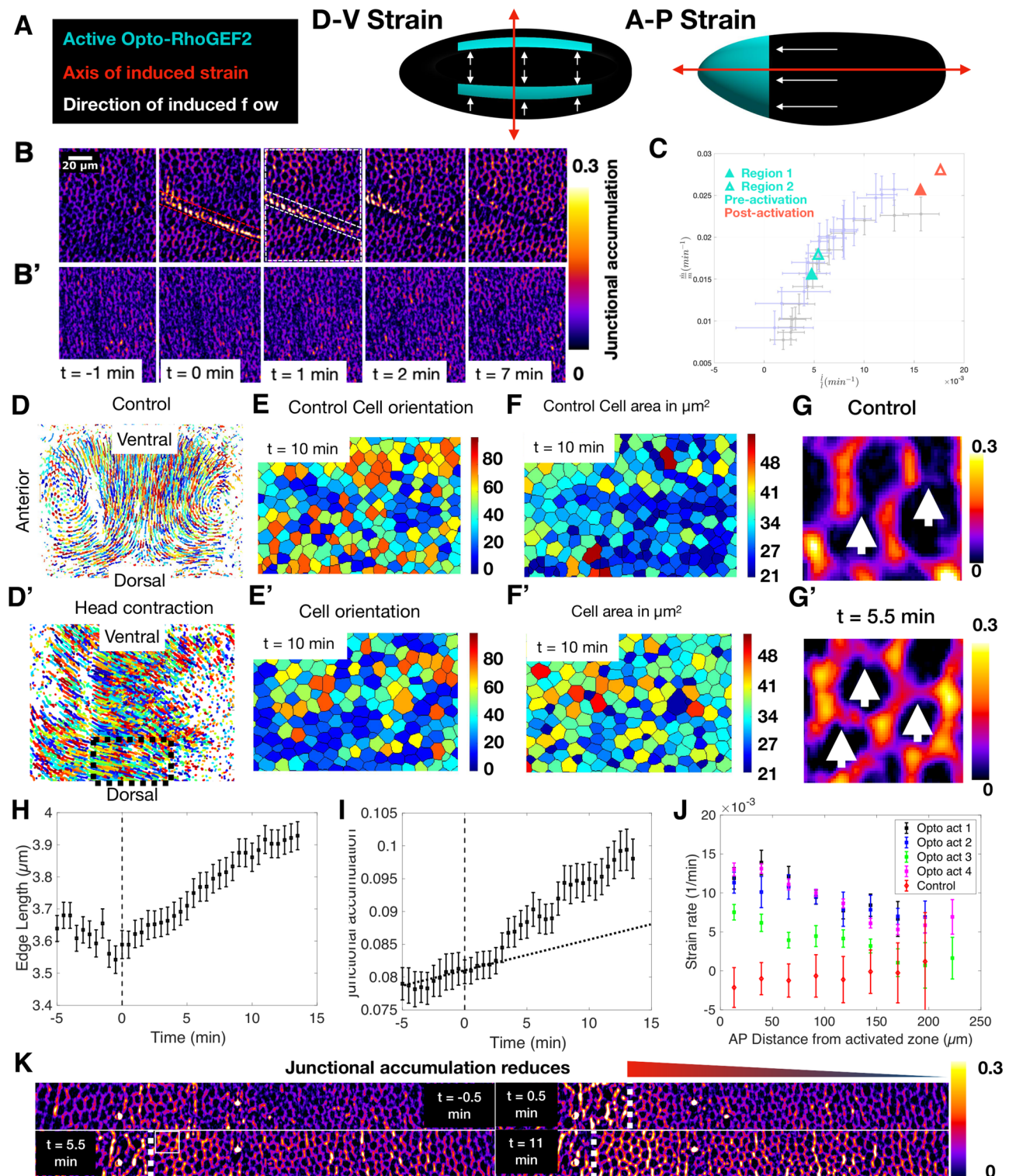
which strain and myosin rates are measured. Dashed lines show the time frame of the fast phase of GBE. **E** JMA across embryo surface (same as shown in **C**). White boxes indicate regions for which the plots are measured. Arrows indicate the earliest time point through which the line fitting the data passes. **F** Cell eccentricity over time in a region corresponding to the central area of the germband (Fig. S1J). **G** Example of cell segmentation and single-edge tracking used to measure strain rate in two regions designated by the white boxes (See Fig. S2 and movie S1 for more tracking). Insets show VF, as in **D**. (**H**, **H'**) Myosin rate (**H**) and strain rate (**H'**) measured along the DV axis for embryo shown in **E**. 0 is ventral midline. (Mean  $\pm$  SD,  $n = 400$  junctions). **I** Plot of strain rate vs. myosin rate in germbands of control embryos, measured as in (**H**, **H'**) (Mean  $\pm$  SD,  $n = 4$  embryos). For a detailed discussion of the number of cell edges per embryo, see Supplementary Information. **D**, **E**, **G**–**I** Source data are provided as a Source Data file.

described previously in ref. 32, this protocol results in two-photon optogenetic activation, allowing for spatially restricted photo-activation patterns to control regional contractility (see Supplementary Methods “Optogenetic activation scheme”). We utilize this strategy to induce strains in various regions and directions and observe the response of myosin.

As shown above, during VF formation, the endogenous patterns of both strain and myosin rates are anisotropic, with much higher values on edges parallel to the DV axis than their orthogonal counterparts. This raises the question of whether mechanical feedback itself is anisotropic. If it is not, the direction of strain has the capacity to affect myosin anisotropy. To distinguish between these two possibilities, we induced strain of cells either along the DV or AP direction. First, we stretched cells along the DV direction, focusing our analysis on the dorsal region. We induced photo-activation in two parallel

regions, extending across the AP axis (Fig. 2A and Fig. S3A–D'). The first time point after activation ( $t = 0$  min) showed a strong signal in the myosin channel, confined to the illumination pattern, resulting from RhoGEF2 recruitment to the membrane and Rho signaling stimulation (Fig. 2B and Fig. S4A–A'). Importantly, in the first 30 s following activation, cells intervening in the two infrared illumination patterns did not show any detectable changes in junctional myosin levels, while myosin signals in the activated regions strongly increased (Fig. S4A, A'). Therefore, we conclude that optogenetic activation remained confined to the infrared illumination pattern and did not activate surrounding cells. Within 1 min, cells in the activated regions contracted (Fig. 2B and Fig. S4A'), and caused a modification of cell flow pattern in non-activated regions (Fig. S4B, B'). While cells remained nearly stationary immediately prior to activation, all cells in the intervening region flowed toward the activation lines and stretched following





activation (Fig. S4A, B'). About 2 min after activation, we observe a pronounced increase in junctional myosin within this region oriented preferentially along the direction of strain (Fig. 2B and Fig. S4A'). In contrast, cells in the same region and developmental time in control embryos showed low accumulation of junctional myosin (Fig. 2B'). Quantitative analysis revealed a significant change in cell shape (Fig. S4C, C'), concomitant with increased myosin recruitment rates to the junction (Fig. S4D, E). Remarkably, the increase in strain rate was matched by a proportional increase in myosin rate, similar to the relationship observed in the whole embryo analysis of VF formation

(Fig. 2B'). However, during VF formation, similarly high strain and myosin accumulation rates were only observed in the close vicinity of the VF but not on the dorsal surface (Fig. 1G, H).

Next, we designed an activation scheme to generate deformations along the AP axis (Fig. 2C and Fig. S3E-H'). Because inducing strain in this direction requires overpowering the underlying flow pattern, we transiently activated RhoGEF2 in the entire head region with the aim to generate a strain of comparable level to that produced during VF invagination along the DV direction. Optogenetic activation resulted in nearly uniform head contraction, producing a striking reorientation of

**Fig. 2 | Patterned contractility by optogenetics redirects flows.** **A** Schematic of optogenetic strategy to generate strain parallel to the DV axis (left) or AP axis (right). Cyan indicates the area(s) of transient optogenetic activation; black regions are not activated. **B** JMA in an activated embryo (as in A, left).  $t = 0$  corresponds to the first image after activation ( $\sim 5$  min post CF formation). Red dashed lines designate the activated regions. **B'** JMA in a control embryo in an equivalent region and developmental stage as that in **B**. **C** Myosin and strain rate for two regions of an activated embryo (Fig. S4A') before (cyan) and after (magenta) activation plotted over control data (from Fig. 1I). **D, D'** Cell trajectories in one lateral side (Fig. S1J) of a control (**D**) and activated (**D'**) embryo for 15 min beginning 5 min after CF formation (first time point following activation in the opto exp). The Black dashed box designates the region analyzed in (**E, F'**). **E, E'** Cells color-coded by orientation (angle between cell long axis and AP axis) in control (**E**) and activated (**E'**) embryos. **F, F'** Cells color coded for apical cell area in control (**F**) and activated (**F'**) embryos. Area distributions are significantly different (Two-sided ks test,  $p = 1.2 \times 10^{-9}$ ). **G, G'** JMA

in equivalent regions of control (**G**) and activated (**G'**) embryos of equivalent developmental time (See **K**). White arrows identify junctions parallel to the AP axis. **H, I** Length (**H**) and JMA (**I**) over time of junctions parallel to the AP axis in an activated embryo. The Gray dashed line shows the time of activation. Data were mean  $\pm$  SD,  $n \geq 200$  junctions. **I** Black dashed line shows JMA expected without activation from the slope of pre-activation data. **J** Strain rate on junctions parallel to the AP axis measured across the entire embryo (excluding the 50-micron region about the ventral midline) as a function of distance from head activation along the AP axis. Data were mean  $\pm$  SD,  $n \geq 200$  junctions. **K** JMA in a lateral region spanning the AP axis of a head activation experiment. The White dashed line shows the boundary between activated (left) and unactivated (right) cells. The white solid outline shows an area corresponding to **G**. Triangle represents the gradation of JMA along the AP axis.  $t = 0$  is first time point after activation,  $-0$  min post CF formation. **H–J** Source data are provided as a Source Data file.

cell flow (Fig. 2D, D'). In control embryos, the primary flow pattern, as established by single-cell tracking, was dominated by cells of the lateral ectoderm flowing towards the ventral midline (Fig. 2D). Head activation caused a global reorientation of flow with cell trajectories pointing towards the head (Fig. 2D'), while retaining a component in the ventral direction due to VF formation. To characterize the effects of this altered flow profile on cell geometry, we quantified cell orientation and area before and after activation. While initially cells were oriented along the DV direction (Fig. 2E), within 10 min of activation, cells on the dorsal side were reoriented along the AP axis, consistent with the pulling direction (Fig. 2E'). Cell area showed a modest, but significant increase after activation (Fig. 2F, F'). Therefore, this activation scheme reorients both cell flow and geometry along the direction of the imposed ectopic strain. It is well established that during GBE, cell interfaces parallel to the AP direction do not accumulate myosin<sup>33</sup>. Indeed, in control embryos, these junctions accumulate very little myosin, such that they were hardly visible relative to perpendicular junctions (Fig. 2G). In contrast, high levels of myosin accumulation on these junctions could be observed in head-activated embryos (Fig. 2G').

Quantitative analysis confirmed that junctions parallel to the ectopic strain direction extend significantly within 1 min after activation and continued to grow at a steady rate for about 8–10 min (Fig. 2H). The rate of myosin accumulation on these junctions was initially very low and similar to that measured on the dorsal surface of control embryos (Fig. 1E, top panel) but increased within 2 to 3 min following activation (Fig. 2I). These results demonstrate a strict temporal sequence of events: (I) accumulation of myosin restricted to the photo-activation domain, (II) contraction of activated cells initiates a change in flow within one minute and alterations of strain rate patterns on edges, and (III) proportionally increased myosin accumulation on strained edges two to three minutes after activation.

Next, we measured the strain rate as a function of distance from the activation front. Adjacent to the activation site, the perturbation drastically increased the strain rate, which gradually decayed towards the posterior pole (Fig. 2J). Depending on the strength of activation, the propagating effects of cell reorientation could still be distinguished for up to 200  $\mu\text{m}$ , corresponding to roughly half the length of the embryo (Fig. 2J). Consistent with this observation, the level of myosin accumulation showed a clear gradient that was higher close to the region of activation and decreased towards the posterior end (Fig. 2K). This gradient in the AP direction recapitulated that observed during VF formation, only rotated 90 degrees in line with the direction of the ectopic strain. In addition to this AP pattern, we also noted that VF invagination induced flow towards the ventral region, causing stretching of junctions parallel to the DV axis (Fig. 2D'). Consistently, we also observed myosin accumulation on junctions parallel to the DV axis characteristic of this stage.

Strain in the direction of the AP axis is normally induced by some morphogenetic processes. For example, after the VF furrow has formed and GBE continues, cells are stretched in the direction of the AP axis, and new cell edges form in this direction as T1 transitions are resolved (Fig. S5A, B). Although the levels of strain generated during this process are substantially lower than those induced by VF formation, using high-resolution confocal microscopy, we are able to measure the junction length changes of nascent DV junctions. Consistent with our observations from optogenetic perturbations, we measure an increase in junctional myosin as the junction extends (Fig. S5C), indicating that our optogenetic results can be generalized to naturally occurring strain rates.

Taken together, these results indicate that strain rate quantitatively affects the pattern of myosin recruitment on both DV and AP junctions. Specifically, the orientation of a junction with respect to the direction of the strain determines the level of junction deformation and, thereby, the level of myosin recruitment. Our results further uncover the long-range consequence of local mechanical perturbations: strain can be transmitted and sensed hundreds of microns away from the source, causing a deformation rate that leads to a proportional increase in the rate of myosin accumulation.

### Strength of feedback depends on DV position but not edge orientation

Our experimental strategy allows us to monitor the response of every junction on the surface to mechanical deformations, prompting us to study mechanical feedback in deeper quantitative detail. The well-established link between cytoskeletal activity and gene expression patterns<sup>9,34</sup>, raises the possibility that genetic patterning regulates mechanical feedback. Such an effect might become visible by studying the proportionality coefficient between strain rate and myosin, which we refer to as the feedback coefficient, as a function of position across the surface of the embryo. A non-uniform coefficient would suggest that the strength of mechanical feedback, and thus the amount of myosin recruited to a given deformation, is patterned.

To explore this possibility, we turn to a more detailed quantitative analysis of the previously described optogenetic experiments to compare the response to deformations on the dorsal vs ventral surface. Our many repetitions of the experiment to generate strain parallel to the DV axis (Fig. 2A) covered a range of DV positions, yet we found that in all cases, strain and myosin rates increased in response to perturbation (Fig. S4G, H). Strikingly, while strain rate showed no correlation with DV position, myosin rate was systematically lower at the dorsal vs. ventral surface (Fig. S4G, H). This suggests the ratio of myosin vs strain rate, and thereby the mechanical feedback coefficient relating these two quantities is graded along the DV axis.

We next further analyzed the experiments in which strain was created parallel to the AP axis (Fig. 2C), and despite nearly uniform



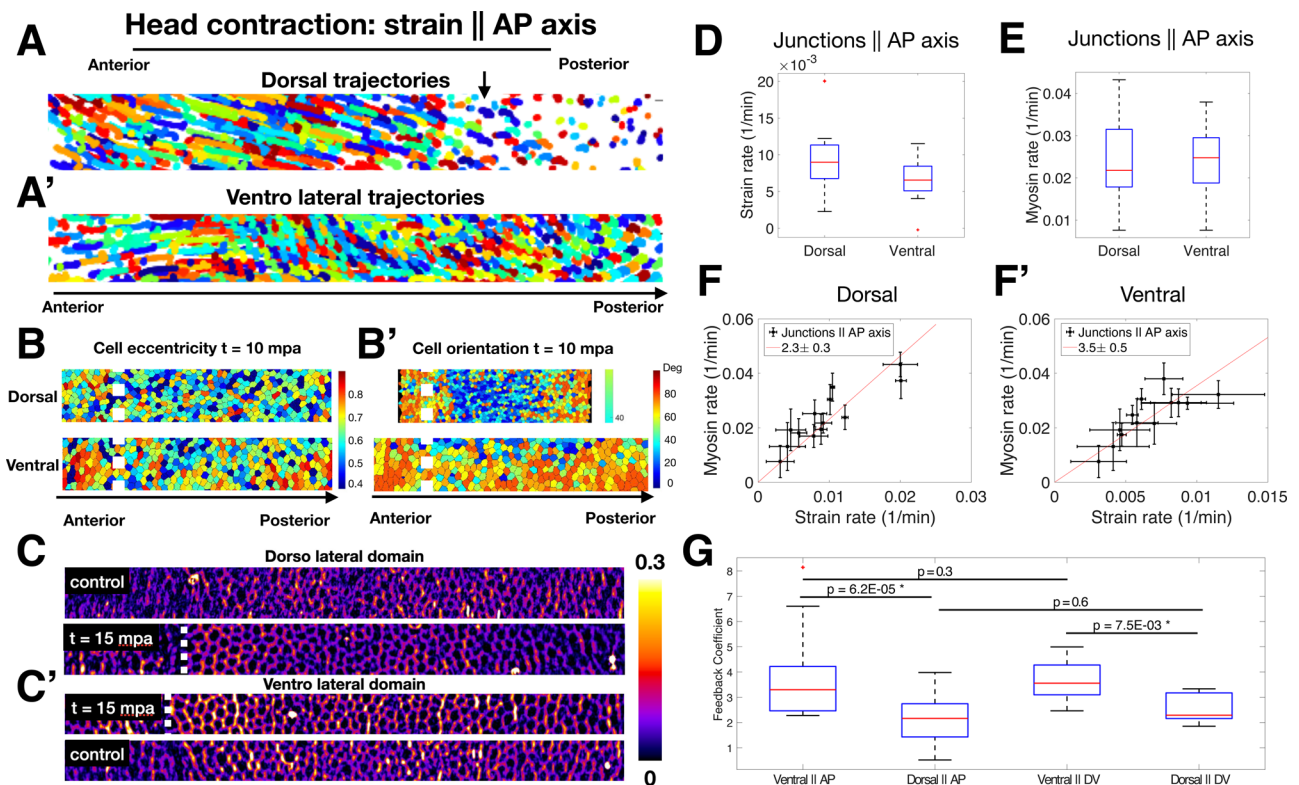


**Fig. 3 | Regional analysis of mechanical feedback coefficient and directionality.** **A, A'** Trajectories of cells tracked for 20 min following head activation in dorsal (**A**) and ventrolateral (**A'**) regions  $\sim 50$   $\mu\text{m}$  wide along the full AP axis. **B** Same regions as (**A**) and (**A'**) 10 min post activation (mpa) color coded for eccentricity. KS test returns the distributions of cell eccentricity are different,  $p = 7.5 \times 10^{-4}$ . **B'** Same regions as (**B**) color coded for orientation of the cell long axis relative to the AP axis. KS test returns distributions of cell orientations are different,  $p = 5 \times 10^{-19}$ . **C** JMA in the dorsolateral region of the control (top) and activated (bottom) embryos at the same developmental stage. **C'** JMA in the ventrolateral region of activated (top) and control (bottom) embryos at the same developmental stage. Regions in **C, C'** are 30  $\mu\text{m}$  wide, spanning the full AP axis. **B, C'** (See Fig. S1J). White dashed line shows the boundary of the activation region in the anterior. **D** Strain

rate in junctions parallel to the AP axis in dorsal and ventral regions following head activation.  $N \geq 200$  per region. **E** Myosin rate on junctions parallel to the AP axis in dorsal and ventral regions. Sample size as in **D**. **D, E** Red line indicates the median, box lower and upper quartiles, whiskers are minimum and maximum. **F, F'** Strain rate vs myosin rate on junctions parallel to the AP axis in the dorsal (**F**) and ventral (**F'**) regions for all head activation experiments,  $N = 5$  embryos. The Red line shows the best-fit proportionality of the data points. The legend shows the feedback coefficient and the 95% confidence interval. Error bars are SEM. **G** Comparison of feedback coefficient based on junction orientation (parallel to DV vs AP) and region (dorsal vs ventral). This coefficient is the proportionality between strain rate vs myosin rate plot as in (**F, F'**), Fig. S4G. **H. P** values are obtained by single-sided Welch  $t$ -test.  $N = 10$ . **D–G** Source data are provided as a Source Data file.

contraction induced along the circumference, we observed striking differences at the dorsal vs. ventral regions, both in terms of cell trajectories (Fig. 3A, A') and cell shapes (Fig. 3B, B'), as well as myosin activation patterns (Fig. 3C, C'). Quantitative analysis focusing only on junctions parallel to the AP axis confirms that junctions on the dorsal surface experience higher strain compared to their counterparts in ventral regions (Fig. 3D). Notably, the myosin rate did not exhibit the same trend, and in fact, the average myosin rate was lower on the dorsal than on the ventral region (Fig. 3E). Analysis of myosin accumulation rate as a function of strain rate for junctions parallel to the AP axis revealed a lower feedback coefficient in dorsal than ventral regions (Fig. 3F, F').

Figure 3G shows a summary of the feedback coefficient quantified as the ratio of myosin rate over strain rate, organized in the four different categories we analyzed: dorsal vs ventral domains, and junctions parallel to AP vs DV axis. These results do not show a significant difference in terms of junction orientation within either the dorsal or ventral region but do across regions. This indicates that mechanical feedback acts independently of junction direction, and that genetically encoded spatial patterning of the mechanical feedback coefficient downstream of positional information determines the amount of myosin recruitment in response to a given deformation.

### Single junction analysis reveals two timescales govern myosin dynamics

The preceding analyses average cell junction strain and myosin rates within local regions of interest and rely on data at 30 s temporal resolution. While this is sufficient to identify the causal relationship between strain and myosin rates, we wanted to analyze the relationship between deformation and myosin at high frequency. We moved to local imaging at higher temporal resolution using confocal microscopy to track both junction length and myosin signal over time. Representative images (Fig. 4A) show a junction marked with both myosin and a membrane marker at successive time points. Single-edge tracking revealed that myosin density on the edge (Fig. 4B) and junction length (Fig. 4B') exhibited rich dynamics with rapid fluctuations around a longer time scale trend. From myosin concentration and junction length, we extracted strain and myosin rates and plotted them as a function of time (Fig. 4C). Myosin and strain rates oscillated out of phase with a period of 74 s (Fig. 4D). Cross-correlation between myosin and the strain rates showed a negative correlation with a time shift of  $-7$  s and a positive correlation with a time shift of 30 s, suggesting close to half a period phase shift. This effect is specific to the relationship between myosin and strain rates, as the cross-correlation between strain rate and the concentration of the membrane marker GAP43:mCherry showed no significant peaks.

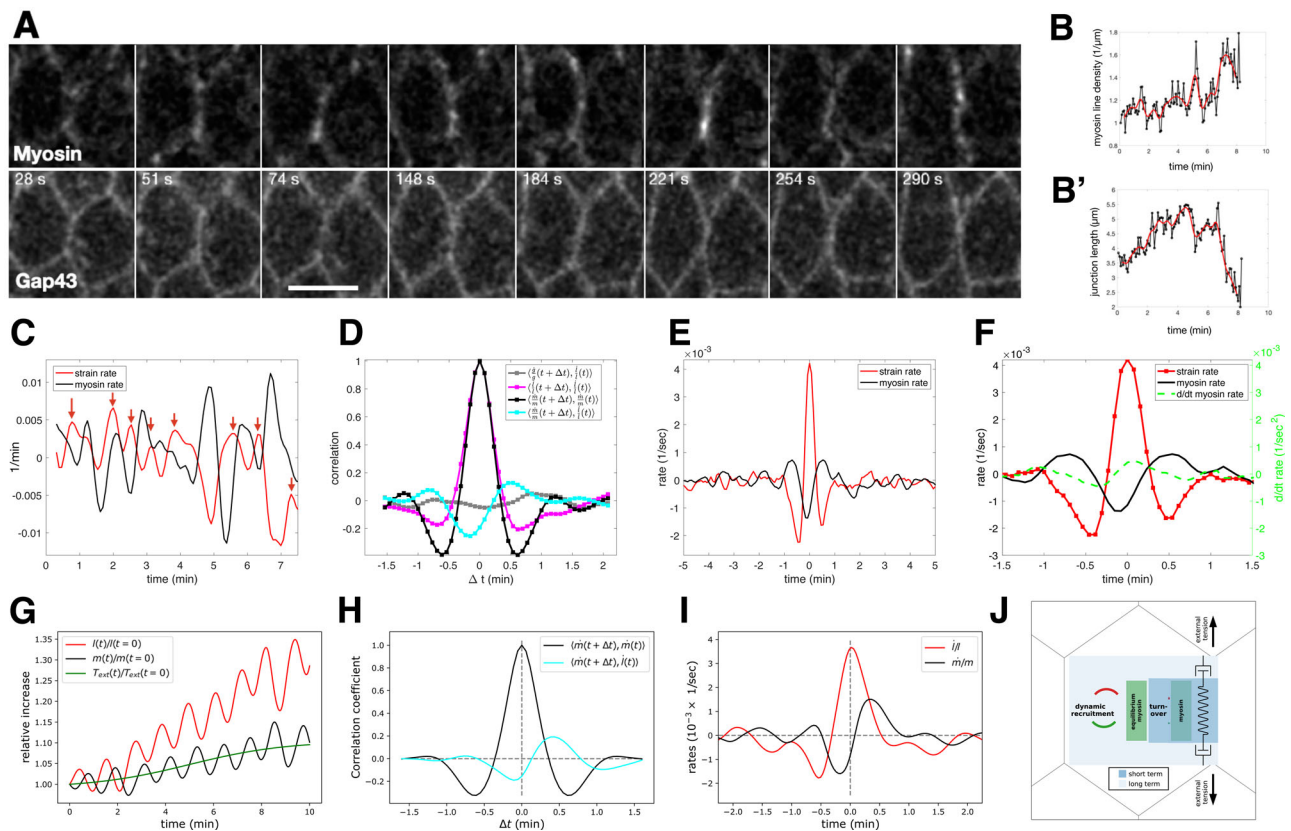


**Fig. 4 | Single-edge analysis and modeling of myosin and membrane dynamics.**

**A** Confocal images of cells during early gastrulation marked with *sqh::GFP* and *Gap43::mCherry* showing time points that highlight the oscillations of myosin and junction length. The scale bar is 5 microns. Representative images are shown from one of eight similar movies. **B** Myosin line density normalized to initial myosin line density over time of data shown in panel (A). **B'** Junction length in microns over time. In both (B, B'), black points represent data. The red line is a gaussian smoothed representation of the raw data points. Sigma = 10 s. **C** Plot of strain rate (red) and myosin rate (black) over time calculated from the data plotted in (B, B'). Red arrows indicate peaks in strain rate. **D** Autocorrelation analysis of strain rate (red) and myosin rate (black) and cross-correlation analysis of membrane rate with strain rate (gray) and myosin rate with strain rate (green). **E** Traces were obtained by

aligning strain rate peaks and averaging the aligned strain rate (red) and myosin rate (black). **F** Same as in E, with displayed data corresponding only to one cycle before and after  $t = 0$  and with the myosin acceleration plotted on the same graph (green dashed line). **D–F** include  $n = 175$  bonds. Similar results have been obtained across five embryos. **G** Sample simulation of the relative increase in junction length (red) and myosin concentration (black) over time given by the model. External tension is applied to the junction shown in green. **H** Autocorrelation analysis of myosin rate (black) and cross-correlation of myosin rate with strain rate (green), based on  $N = 500$  model simulation runs. **I** Average curves of strain rate (red) and myosin rate (black) predicted by the model after strain rate peak alignment, as in E ( $N = 500$ ). **J** Cartoon representation of the dilution oscillator model with mechanical feedback. **C–I** Source data are provided as a Source Data file.

To characterize the longer-term impact of strain rate on myosin on the same junction, we investigated the typical response of myosin rate to significant peaks in the strain rate (red arrows in Fig. 4C) by averaging the time traces of multiple edges centered around peaks (Fig. 4E, F). We focused on the fluctuating forces acting on tracked junctions to investigate the consequences of peaks in the strain rate. The average strain rate around the peak has, as expected, a global maximum at 0 and two adjacent minima symmetrically localized around plus/minus 30 s. The average myosin rate exhibited a global minimum shortly before the strain rate peaks, as expected from the cross-correlation analysis. The peaks of myosin appeared symmetrical both in timing as well as magnitude. The situation was different for the minima. While the last minimum in myosin rate appeared 74 s before the peak, the first minimum after the peak did not appear until 106 s. This suggests a prolonged phase of myosin sourcing in response to deformation. Indeed, the time derivative of the myosin rate became positive as soon as the junction extended, signified by a positive strain rate (Fig. 4F). Taken together, these findings indicate that myosin is subject to two separate timescales: rapid fluctuations around a slowly changing reference value set by mechanical-driven recruitment, similar to theoretical ideas proposed in ref. 35.

To quantitatively explore this hypothesis, we formulated a physical model with few parameters. We adapted a “concentration oscillator” model, which has been shown to capture the dynamics of apical myosin and cell area fluctuations<sup>36</sup>, by incorporating a mechanical feedback mechanism, which was proposed as a requirement to maintain the mechanical stability of tissues<sup>13</sup>, see Supplementary Note 1 for more detail. With this model, we could capture both the short-term oscillations observed in the single-edge dynamics as well as the long-term drift in junction rest length and myosin levels (Fig. 4G). We assumed that at short timescales, a cell edge behaves as an elastic spring that can elongate under external tension or shorten, based on the balance of external forces, elasticity, and actomyosin contractility. Oscillations between these two states are sustained by the effects of dilution, concentration, and myosin turnover, which are captured by the concentration oscillator. Simulating the autocorrelation and cross-correlation analysis using this model accurately recreated the measures above (Fig. 4H). At longer timescales, the cell edge undergoes viscoelastic relaxation due to cytoskeletal remodeling, allowing for changes in the junction rest length. Mechanical feedback causes the recruitment of myosin in proportion to the edge strain, which balances the external tension to stabilize junction length, leading to plastic deformation and adjusted equilibrium myosin levels (Fig. 4G). By



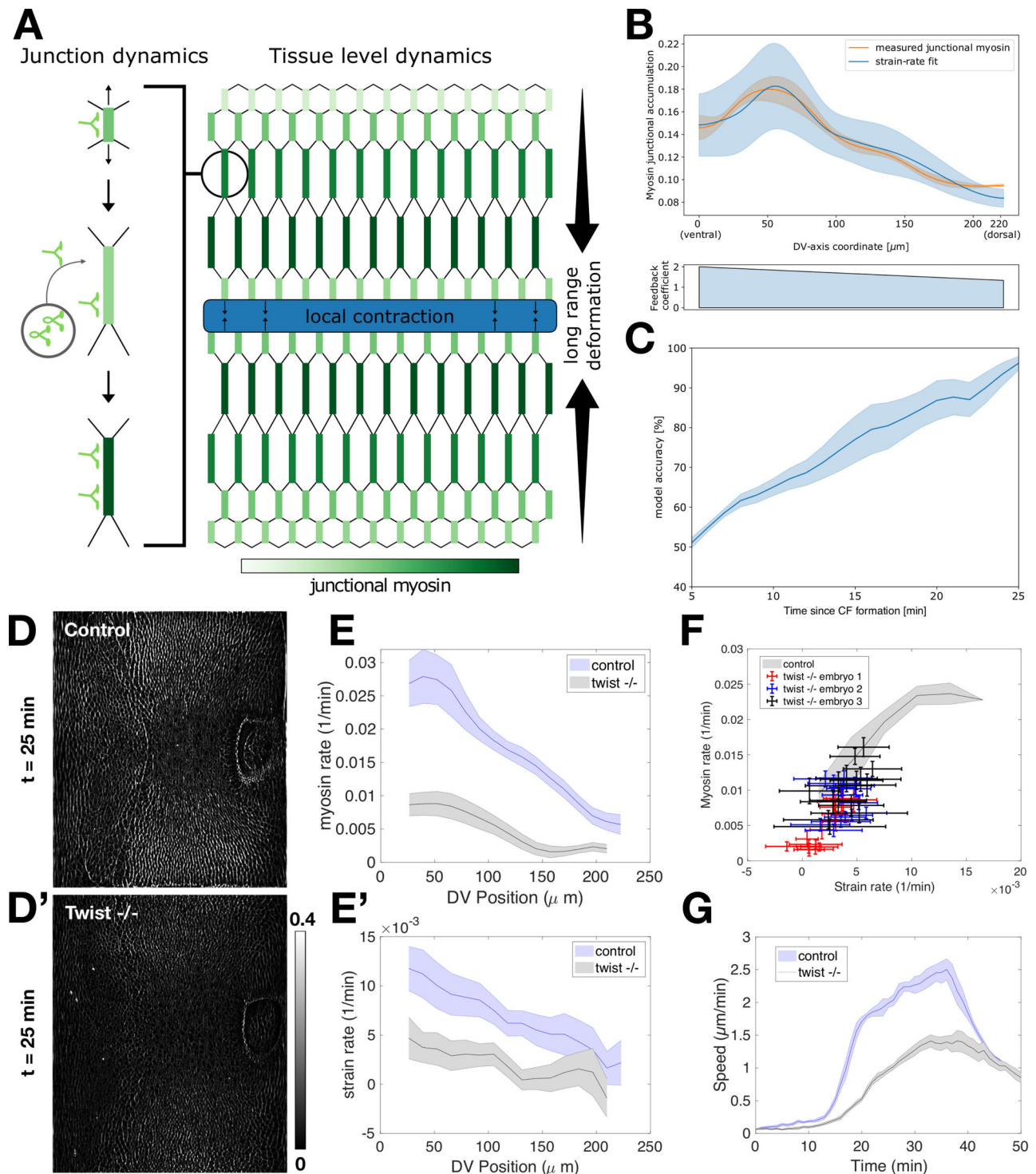


**Fig. 5 | Prediction of embryo-scale myosin distribution from junctional model and analysis of twist mutant embryos.** **A** Illustration connecting junctional dynamics (left) with tissue-scale dynamics (right). Local contraction propagates across the tissue as long-range deformations, which serve as the source of external tension activating mechanical feedback for myosin recruitment and establishing tissue-scale gradients of junctional myosin accumulation. **B** Comparison of measured junctional myosin levels (orange) and myosin levels predicted from the model using total strain as input (blue). The lower plot shows the DV gradient of the feedback coefficient input into the model. Error bars give the standard deviation of model output (i.e. (total strain)<sup>2</sup> feedback coefficient) over tracked junctions. **C** Model accuracy over time, representing the level of agreement between

predicted and measured myosin profiles. **D, D'** Junctional myosin accumulation in twist heterozygous ("control", **D**) and twist homozygous ("Twist <sup>-/-</sup>", **D'**) embryos at equivalent times. The lookup table is the same for **D, D'**. **E** Myosin rate as a function of DV position in control (blue) and twist (black) embryos. **E'** Strain rate as a function of DV position for control (blue) and twist (black) embryos. **F** Strain rate vs myosin rate plot with the average wild-type curve (blue) and individual twist mutant embryos (points). **G** Mean velocity over time for wildtype and twist mutant embryos.  $t = 0$  corresponds to the onset of CF formation. In all cases, error bars indicate standard deviation, unless otherwise stated. **B, C, E-G** Source data are provided as a Source Data file.

modeling these behaviors, we were able to recreate the peak-aligned strain rate and myosin rate curves, including key features such as the phase-shifted oscillations and asymmetry about zero in both curves (Fig. 4I). Notably, a concentration oscillator model alone, without mechanical feedback, was insufficient to account for this observation (Fig. S7C). In summary, external tension on a junction influences myosin dynamics at two timescales: fast turnover characterized by oscillatory behavior without net gain of myosin, and slower adjustment of myosin levels due to mechanical feedback (Fig. 4J and S7A, see SI for more detail). Taken together, the high-frequency analysis of single junctions and the accuracy with which our model reproduces these dynamics support the mechanism for dynamic myosin recruitment identified through our analysis of wildtype and optogenetic whole embryo live imaging data.

### Embryo-scale myosin levels can be accurately predicted from integrated strain rate

Next, we wanted to test if our single junction model could be used to account for the early myosin dynamic patterns established during VF formation at the whole embryo scale. Because the myosin accumulation rate is likely influenced by factors other than strain rate, it remains unclear if the predictive power of mechanical feedback will extend to the large-scale and long-time pattern of myosin dynamics, when the anisotropic pattern characteristic of GBE is established. i.e., during the 20 min following cephalic furrow formation. By integrating the deformation rates of individual junctions, we used our model to provide a quantitative estimate of the contribution from mechanical feedback to the time course of myosin on junctions. As shown in Fig. 1C, the myosin pattern exhibited a striking gradient along the DV axis. On the scale of single-cell edges, our model predicts that a junction elongating under external tension will undergo a net increase in myosin levels due to mechanical feedback (Fig. 5A, left). Local contraction in a mechanically coupled epithelium will generate external tension on junctions surrounding the site of contraction (Fig. 5A, right). This effect decays with distance from the source of contraction, resulting in a gradient of external tension. Junctions with orthogonal orientation to the contraction pattern will thus experience an unbalanced external tension, extend, and recruit myosin (Fig. 5A, right).

We used single-edge tracking to reconstruct the history of deformations experienced by individual edges across the DV axis (Fig. S2A, B). The myosin profile at any given time was quantified using the junctional accumulation measure (Fig. 1C). Our model relates myosin dynamics to deformations by the feedback coefficient, which varies across the surface (Fig. 3I). Therefore, we measured all spatially varying observables relevant to predicting the myosin profile from deformation rates, leaving only a single fitted constant in the integrated feedback law (see Supplementary Note 1 for more detail). The predicted profile and the measured myosin were remarkably similar (Fig. 5B). Agreement between our prediction and the observed myosin pattern is initially low, due to the overall low strain and myosin levels at early time points, but rapidly increased to ~80% just before the onset of GBE when myosin accumulation is highest, (Fig. 5C). This suggests our model is highly accurate both at the level of individual junctions and across the entire DV axis.

This level of predictive power indicates that during GBE, myosin distribution strongly depends on strain pattern. Because VF invagination is a major source of deformation in the early embryo, it is expected to contribute significantly to the generation of strain. Indeed, previous work has reported lower strain rates and cell intercalation rates in *twist* mutants<sup>21</sup>, which has been further corroborated by a recent work demonstrating reduced elongation rates, cell shape change, and cell exchange rates in these mutants<sup>37</sup>. We, therefore, take advantage of these changes in *twist* embryos to determine the effects on the myosin profile. This can be tested in mutants affecting VF formation, such as loss of function alleles of the transcription factor Twist.

*twist* mutant embryos still exhibit residual cell behaviors that are hallmarks of VF formation. The high resolution of our analysis pipeline at the whole embryo level allowed us to exploit this detail in a quantitative test of our model. In *twist* mutants, Snail expressing cells in the ventral region undergo pulsed apical contractions, without intervening stabilization of the apical surface<sup>34</sup>. This suggests these cells can still pull on the adjacent germband, albeit less effectively than their WT counterparts. We, therefore, expect a quantitatively reduced profile of deformations and accordingly predict a reduced myosin profile. Indeed, the levels of junctional myosin accumulation during early GBE were significantly reduced in *twist* mutants compared to wild-type embryos at an equivalent developmental stage (Fig. 5D, D'). Both myosin rates (Fig. 5E) and strain rates (Fig. 5E') were 2.5 times lower and displayed shallower gradients in *twist* mutants. When plotting myosin rates vs strain rates, the *twist* data followed the same curve as their WT counterparts, although at lower strain and myosin rates (Fig. 5F), indicating that the mechanisms underlying this proportionality were preserved in *twist* mutants. Of note, we find similar results for snail mutants that also lack ventral furrows (Fig. S6B). The mechanical consequences of the reduced myosin rate, and hence reduced myosin DV gradient, were apparent when comparing the mean velocity profile in wildtype and *twist* embryos. This analysis revealed that the magnitude of flow during GBE, particularly during the fast phase, was also reduced by the same factor of 2.5 (Fig. 5G). Despite the lower magnitude of flow, the direction of the flow pattern is largely maintained in *twist* embryos, such that GBE proceeds, albeit markedly slower. *Twist* mutants, therefore, fully elongate their germbands, as previously reported in ref. 38, but the reduced kinetics mean that *twist* mutants take longer to reach the same elongation length as their wild-type counterparts. This remarkable quantitative agreement strongly suggests that deformation rates underlie the establishment of the early DV myosin gradient, which sets the pace of germband extension.

## Discussion

Here we combined light sheet microscopy with physiological deformations afforded by patterned optogenetic contractility, to demonstrate a mechanical feedback mechanism, which results in dynamic myosin recruitment to junctions proportional to the rate of edge deformation. Our data show that mechanical feedback is isotropic and patterned along the DV axis. High-frequency analysis of individual cell junctions combined with a physical model revealed the dynamic nature of myosin on adherens junctions: similar to medial pools on the apical and basal cell surface, the junctional myosin concentration oscillates around a mean value. We show that the dynamics of this mean value can be quantitatively captured by a mechanical feedback mechanism which responds to the rate of edge strain. Our model also quantitatively bridges the junctional scale to the global embryo scale, predicting the establishment of in toto myosin profiles from measured deformations. This level of predictive power is surprising, as genetic evidence in fixed samples demonstrates that pair-rule genes affect myosin anisotropy via a recently discovered toll receptor code<sup>9</sup>, yet we have not explicitly accounted for any AP patterning in our model.

Our analysis of myosin dynamics further reveals that the strength of mechanical feedback is globally graded and patterned. This suggests that genetic patterning provides positional information to set the stage for the mechanical feedback capacity of individual cells. In the context of gastrulation, these results suggest that patterning of the feedback coefficient along the DV axis acts as a developmentally planned physical mechanism for symmetry breaking, ensuring robust and globally graded myosin distribution. Reducing the DV gradient of the myosin profile reduces the speed of GBE accordingly.

Our optogenetic perturbations argue that the cytoskeleton plays a permissive role in the establishment of mechanical feedback in all directions, indicating that the molecular components of this mechanism are likely uniformly distributed at the cell surface.

Intriguingly, Toll receptors are distributed uniformly<sup>10</sup>, yet the mechanism that produces an anisotropic myosin distribution from this isotropic Toll distribution is an open question. A recent review<sup>2</sup> has described this gap in the model and proposed several possibilities. Our data suggest an additional mechanism that warrants further exploration: mechanical feedback bridges the discrepancy in the current model between isotropic Toll distribution and anisotropic myosin distribution downstream of Tolls. In this scenario, strain anisotropy leads to anisotropic activation of an isotropic mechanical feedback pathway, potentially involving Toll receptors, to establish the anisotropic myosin distribution. The anisotropic strain rate needed for this effect is caused by the internalization of around 1000 cells at the ventral pole of the embryo. Together with patterning the feedback coefficient along the DV axis, this mechanism contributes to establishing a global myosin anisotropy gradient that drives germband extension flow.

Future studies combining dynamic analysis with genetic perturbations of the pair-rule genes and their targets may help reach a unified quantitative model of cytoskeletal dynamics during *Drosophila* gastrulation. Despite the Arthropod specific role of Tolls, the highly conserved morphogenetic processes of apical constriction and cell intercalation driving VF formation and GBE<sup>39,40</sup>, respectively, raise the possibility that the mechanism we describe here may have implications for the development of a wide variety of species employing these modules. It is, therefore, intriguing to note a dual role for mechanics in development: not only as the set of physical properties that determine how tissues deform, but also as a genetically encoded physical mechanism to ensure robust tissue flow.

## Methods

### Light sheet microscopy

We used a custom-built multi-view selective plain illumination microscope (MuVI SPIM)<sup>29</sup> in a scatter-reducing imaging mode<sup>25</sup> for fluorescent-based live imaging of full *Drosophila* embryos at sub-cellular resolution. Briefly, the setup involves a pair of orthogonally arranged illumination and detection arms, in duplicate arranged such that illumination and detection face one another. For illumination, we used a custom-built laser combiner that housed a set of continuous wave laser lines (488, 561, and 660 nm), all OBIS LX, Coherent Inc. These laser lines were always operating at the same set output power for each experiment. The stability of the beam was assessed using an optical power meter from Thorlabs (PMD 100D with S121C). These laser lines were combined using dichroic mirrors on kinematic mirror mounts. A broadband beam splitter from Omega Optical Inc., designed to evenly split the beam at 488, 561, and 940 nm (for use in conjunction with optogenetic activation, see below), was used to duplicate the light path for feeding the two illumination arms. The light paths in each illumination arm were identical. They first consisted of a pair of kinematic mirrors for alignment purposes, a galvanometric mirror (Cambridge technology), a scan lens (Sill Optics), a Tube lens (200 mm focal length), and a water-dipping objective (CFI Plan Fluor 10x, NA 0.3, Nikon). The detection involves a water-dipping objective (APO LWD 25x, NA 1.1, Nikon), a filter wheel (Lambda, Sutter Instruments) with emission filters (FF01-542/27-25, FF01-609/62-25, BLP01-568R-25, BLP01-664R-25, all Semrock), tube lens (200 mm focal length), and an sCMOS camera (Hamamatsu ORCA-Flash 4.0 V3).

For optimal image quality, we reduced optical scattering, following the strategy outlined in ref. 25. Briefly, we used a National Instruments Multi-function I/O card (PCI-6229) to generate a sequence of electronic signals to synchronize galvanometric mirror phase with the start of the image acquisition, and sample motion. The camera was operated light-sheet mode readout, at maximum speed setting for the acquisition front. The width of exposing pixels around this form was set to 52 pixels (corresponding to an effective 13.4  $\mu\text{m}$ ) in all experiments.

Optical sectioning involved electronically controlled stages, all from Physik Instrumente GmbH and Co.Kg. A translation stage (linear piezo stage P-629.1 cd with E-753 controller), a rotational piezo stage (U-628.03 with C-867 controller), and a linear actuator (M-231.17 with C-863 controller).

The electronic acquisition was controlled through micro manager<sup>41</sup>.

### Optogenetic activation

For tight spatial confined optogenetic activation, we took advantage of the two-photon effect described for fluorescence microscopy in ref. 42. This non-linear method uses a high-intensity infrared laser to allow for spatially restricted activation of a fluorophore or optogenetic constructs and is widely used in deep tissue imaging, e.g., neuroscience<sup>26,43</sup>. Briefly, specificity is achieved because excitation of the chromophore requires simultaneous absorption of two infrared photons instead of one photon of approximately half the wavelength normally employed. The energies required for a non-zero cross-section of this event are only achieved in the focal spot of the objective. This effect, therefore, drastically reduces light scattering, thus avoiding optogenetic activation away from the focal plane of the objective. We used a tuneable femtosecond laser (Chameleon Vision II laser system, Coherent Inc.), set to 940 nm for spatially controlled activation.

### Image acquisition

Embryos were dechorionated following standard procedures and mounted in agarose gels as previously described<sup>29</sup>. Imaging proceeds as follows: the embryo is imaged simultaneously from two objectives with sections spaced 1.5  $\mu\text{m}$  apart, producing two separate Z stacks from opposite sides of the embryo. The embryo is rotated by 45 degrees and imaged again for three additional positions, for a total of eight views per time point. Total imaging duration per time point is ~18 s allowing for temporal resolution of 30–60 s.

### Data fusion

Fluorescent beads (Fluoresbrite multicolor fluorescent 0.5- $\mu\text{m}$  beads 24054, Polysciences Inc.) are diluted 1:1000 in 1% low-melting point agarose solution into which the embryo is mounted for imaging. These fluorescent beads serve as fiducial markers to register views using interest point detection and matching with the Fiji plugin Multi-view Reconstruction<sup>44</sup>. The difference in the Gaussian interest point detection method is used to identify the bead locations in all views for all time points. Beads are matched using the fast 3D geometric hashing (rotation invariant) algorithm and all-to-all time point matching (global optimization). The views are then registered using an affine transformation model regularized to a rigid model with a lambda value of 0.10. Images are fused using Multi-view deconvolution with an efficient Bayesian iteration. The PSF estimation is extracted from the beads. The resulting image has an isotropic resolution of 0.2619  $\mu\text{m}$ .

### Surface of Interest extraction

Tissue cartography was used to define SOI and extract fluorescence data on pullbacks<sup>45</sup>. The embryo surface is determined using the Ilastik detector, giving rise to a point cloud for SOI construction. This point cloud is fitted by using the sphere-like fitter class, to create a smooth representation of the SOI using cylinder coordinates defined by AP and DV axes.

### Confocal imaging

Embryos were dechorionated, mounted on a glass bottom MaTek dish, and covered with water. Embryos were imaged with a Leica SP8 confocal microscope (HC PL Apo CS2 40x, NA 1.1, Water, Leica Inc.) An image stack corresponding to the apical surface (nine stacks with 1  $\mu\text{m}$  axial resolution, 0.08  $\mu\text{m}$  lateral resolution) was acquired every



4.6–4.8 s during the time just before ventral furrow formation through the fast phase of GBE.

### Optogenetics crosses

Crosses between UASp>CIBN::pmGFP; UASp>Cry2::RhoGEF2 virgins, and sqh::mCherry/Cyo; osk>Gal4/TM3 males were set up and kept in the dark at 25 °C. All subsequent procedures were performed using only red-light illumination. F1 progeny of the appropriate genotype were sorted and maintained in an embryo-collecting cage. See Supplementary Information for more details.

### Segmentation and cell edge tracking

For the segmentation of cell outlines, a layer approximately 5 μm below the SOI was segmented using Ilastik<sup>46</sup>. The image mask generated from this workflow allows for edge detection and tracking using procedures outlined in ref. 47, implemented in a custom MatLab script, from which edge length and myosin intensity are measured. All measurements involve the metric tensor to correct for possible distortions from projections in maps<sup>45</sup>. See Supplementary Information for more detail.

### Mean velocity

Flow fields were calculated using particle image velocimetry (PIV)<sup>48</sup>. An ensemble average flow field for each genotype was calculated by time aligning the individual datasets (5 twist± and 5 twist -/-) and calculating the average flow field. From this ensemble-averaged flow field, the average velocity was calculated for each time point. (See “Reproducibility of the morphogenetic flow” in ref. 4 for details.)

### Fly lines

*Df(2L)dpp[s7-dp35] 21F1-3;22F1-2 (halo), twi<sup>95/53</sup>/Cyo,sqh>sqh::GFP<sup>34</sup>*  
*Df(2L)dpp[s7-dp35] 21F1-3;22F1-2 (halo), sna<sup>1605</sup>/Cyo,sqh>sqh::GFP<sup>34</sup>*

w[\*]; sqh>GAP43::mCherry(attp40)/Cyo; sqh>sqh::GFP<sup>49</sup>  
w[\*]; P[w +, UASp>CIBN::pmGFP]/Cyo; P[w +, UASp>RhoGEF2-CRY2]/TM3,Ser<sup>26</sup>  
w[\*]; P[w +, sqh>sqh::mCherry]/Cyo; P[w +, Osk>Gal4::VP16]/TM3,Ser<sup>26</sup>

Twist and Snail mutant embryos

Twist and Snail mutant fly lines carry the halo mutation on the same chromosome as the mutation of interest. Mutant embryos are selected from the progeny by selecting for the halo mutant phenotype under halocarbon oil on a dissecting scope. Mutations are confirmed by the absence of VF using whole embryo time-lapse imaging on the MuVi SPIM as described.

### Reporting summary

Further information on research design is available in the Nature Portfolio Reporting Summary linked to this article.

### Data availability

Source data are provided with this paper. Light sheet microscopy datasets exceed multiple gigabyte, and will be made available upon reasonable request. Source data are provided with this paper.

### References

- Gilmour, D., Rembold, M. & Leptin, M. From morphogen to morphogenesis and back. *Nature* **541**, 311–320 (2017).
- Paré, A. C. & Zallen, J. A. Cellular, molecular, and biophysical control of epithelial cell intercalation. *Curr. Top. Dev. Biol.* **136**, 167–193 (2020).
- Collinet, C. & Lecuit, T. Programmed and self-organized flow of information during morphogenesis. *Nat. Rev. Mol. Cell Biol.* **22**, 245–265 (2021).
- Streichan, S. J., Lefebvre, M. F., Noll, N., Wieschaus, E. F. & Shraiman, B. I. Global morphogenetic flow is accurately predicted by the spatial distribution of myosin motors. *eLife* **7**, 159 (2018).
- Heer, N. C. et al. Actomyosin-based tissue folding requires a multicellular myosin gradient. *Development* **144**, 1876–1886 (2017).
- Dicko, M. et al. Geometry can provide long-range mechanical guidance for embryogenesis. *PLoS Comput. Biol.* **13**, e1005443 (2017).
- Saadaoui, M., Rocancourt, D., Roussel, J. & Corson, F. A tensile ring drives tissue flows to shape the gastrulating amniote embryo. *Science* **367**, 453–458 (2020).
- Irvine, K. D. & Wieschaus, E. Cell intercalation during *Drosophila* germband extension and its regulation by pair-rule segmentation genes. *Development* **120**, 827–841 (1994).
- Zallen, J. A. & Wieschaus, E. Patterned gene expression directs bipolar planar polarity in *Drosophila*. *Dev. Cell* **6**, 343–355 (2004).
- Paré, A. C. et al. A positional Toll receptor code directs convergent extension in *Drosophila*. *Nature* **515**, 523–527 (2014).
- Lavalou, J. et al. Formation of polarized contractile interfaces by self-organized Toll-8/Cir1 GPCR asymmetry. *Dev. Cell* **56**, 1574–1588.e7 (2021).
- Fernandez-Gonzalez, R., de Matos Simoes, S., Röper, J.-C., Eaton, S. & Zallen, J. A. Myosin II dynamics are regulated by tension in intercalating cells. *Dev. Cell* **17**, 736–743 (2009).
- Noll, N., Mani, M., Heemskerk, I., Streichan, S. J. & Shraiman, B. I. Active tension network model suggests an exotic mechanical state realized in epithelial tissues. *Nat. Phys.* **13**, 1221–1226 (2017).
- Chanet, S. et al. Actomyosin meshwork mechanosensing enables tissue shape to orient cell force. *Nat. Commun.* **8**, 1–13 (2017).
- Munjal, A., Philippe, J.-M., Munro, E. & Lecuit, T. A self-organized biomechanical network drives shape changes during tissue morphogenesis. *Nature* **524**, 351–355 (2015).
- Acharya, B. R. et al. A mechanosensitive rhoA pathway that protects epithelia against acute tensile stress. *Dev. Cell* **47**, 439–451.e7 (2018).
- Cavanaugh, K. E. et al. Force-dependent intercellular adhesion strengthening underlies asymmetric adherens junction contraction. *Curr. Biol.* **32**, 4779 (2022).
- De Las Bayonas, A. G., Philippe, J.-M., Lellouch, A. C. & Lecuit, T. Distinct RhoGEFs activate apical and junctional contractility under control of G proteins during epithelial morphogenesis. *Curr. Biol.* **29**, 3370–3385.e7 (2019).
- Blanchard, G. B. et al. Tissue tectonics: morphogenetic strain rates, cell shape change and intercalation. *Nat. Methods* **6**, 458–464 (2009).
- Trepast, X. et al. Physical forces during collective cell migration. *Nat. Phys.* **5**, 426–430 (2009).
- Butler, L. C. et al. Cell shape changes indicate a role for extrinsic tensile forces in *Drosophila* germ-band extension. *Nat. Cell Biol.* **11**, 859–864 (2009).
- Collinet, C., Rauzi, M., Lenne, P.-F. & Lecuit, T. Local and tissue-scale forces drive oriented junction growth during tissue extension. *Nat. Cell Biol.* **17**, 1247–1258 (2015).
- Bailles, A. et al. Genetic induction and mechanochemical propagation of a morphogenetic wave. *Nature* **572**, 467–473 (2019).
- Roca-Cusachs, P., Conte, V. & Trepast, X. Quantifying forces in cell biology. *Nat. Cell Biol.* **19**, 742–751 (2017).
- de Medeiros, G. et al. Confocal multiview light-sheet microscopy. *Nat. Commun.* **6**, 1–8 (2015).
- Izquierdo, E., Quinkler, T. & De Renzis, S. Guided morphogenesis through optogenetic activation of Rho signalling during early *Drosophila* embryogenesis. *Nat. Commun.* **9**, 2366 (2018).
- Rauzi, M. et al. Embryo-scale tissue mechanics during *Drosophila* gastrulation movements. *Nat. Commun.* **6**, 8677 (2015).



28. Lye, C. M. et al. Mechanical coupling between endoderm invagination and axis extension in *Drosophila*. *PLoS Biol.* **13**, e1002292–27 (2015).
29. Krzic, U., Gunther, S., Saunders, T. E., Streichan, S. J. & Hufnagel, L. Multiview light-sheet microscope for rapid in toto imaging. *Nat. Methods* **9**, 730–733 (2012).
30. Bertet, C., Sulak, L. & Lecuit, T. Myosin-dependent junction remodeling controls planar cell intercalation and axis elongation. *Nature* **429**, 667–671 (2004).
31. Guglielmi, G., Barry, J. D., Huber, W. & De Renzis, S. An optogenetic method to modulate cell contractility during tissue morphogenesis. *Dev. Cell* **35**, 646–660 (2015).
32. Guglielmi, G. & De Renzis, S. Optogenetic inhibition of apical constriction during *Drosophila* embryonic development. *Methods Cell Biol.* **139**, 167–186 (2017).
33. Rauzi, M., Verant, P., Lecuit, T. & Lenne, P.-F. Nature and anisotropy of cortical forces orienting *Drosophila* tissue morphogenesis. *Nat. Cell Biol.* **10**, 1401–1410 (2008).
34. Martin, A. C., Kaschube, M. & Wieschaus, E. F. Pulsed contractions of an actin-myosin network drive apical constriction. *Nature* **457**, 495–501 (2009).
35. Odell, G. M., Oster, G., Alberch, P. & Burnside, B. The mechanical basis of morphogenesis: I. Epithelial folding and invagination. *Dev. Biol.* **85**, 446–462 (1981).
36. Dierkes, K., Sumi, A., Solon, J. & Salbreux, G. Spontaneous oscillations of elastic contractile materials with turnover. *Phys. Rev. Lett.* **113**, 148102 (2014).
37. Wang, X. et al. Anisotropy links cell shapes to tissue flow during convergent extension. *Proc. Natl Acad. Sci. USA* **117**, 13541–13551 (2020).
38. Leptin, M. & Grunewald, B. Cell shape changes during gastrulation in *Drosophila*. *Development* **110**, 73–84 (1990).
39. Tada, M. & Heisenberg, C.-P. Convergent extension: using collective cell migration and cell intercalation to shape embryos. *Development* **139**, 3897–3904 (2012).
40. Heisenberg, C.-P. & Bellaïche, Y. Forces in tissue morphogenesis and patterning. *Cell* **153**, 948–962 (2013).
41. Edelstein, A. D. et al. Advanced methods of microscope control using  $\mu$ Manager software. *J. Biol. Methods* **1**, 10–10 (2014).
42. Denk, W., Strickler, J. H. & Webb, W. W. Two-photon laser scanning fluorescence microscopy. *Science* **248**, 73–76 (1990).
43. Liu, R., Li, Z., Marvin, J. S. & Kleinfeld, D. Direct wavefront sensing enables functional imaging of infragranular axons and spines. *Nat. Methods* **16**, 615–618 (2019).
44. Preibisch, S., Amat, F., Stamatakis, E., Sarov, M. & Singer, R. H. Efficient Bayesian-based multiview deconvolution. *Nat. Methods* **11**, 645–648 (2014).
45. Heemskerk, I. & Streichan, S. J. Tissue cartography: compressing bio-image data by dimensional reduction. *Nat. Methods* **12**, 1139–1142 (2015).
46. Sommer, C., Straehle, C., Köthe, U. & Hamprecht, F. A. Ilastik: interactive learning and segmentation toolkit. In *2011 IEEE International Symposium on Biomedical Imaging: From Nano to Macro* 230–233 (IEEE, 2011).
47. Streichan, S. J., Hoerner, C. R., Schneidt, T., Holzer, D. & Hufnagel, L. Spatial constraints control cell proliferation in tissues. *Proc. Natl Acad. Sci. USA* **111**, 5586–5591 (2014).
48. Adrian, R. J. Twenty years of particle image velocimetry. *Exp. Fluids* **39**, 159–169 (2005).
49. Martin, A. C., Gelbart, M., Fernandez-Gonzalez, R., Kaschube, M. & Wieschaus, E. F. Integration of contractile forces during tissue invagination. *J. Cell Biol.* **188**, 735–749 (2010).

## Acknowledgements

We thank E. Izquierdo, D. Krüger, M. Lefebvre, N. Noll, B. Shraiman, E. Wieschaus, past and present members of the Streichan lab for helpful discussions. We thank E. Wieschaus for snail and twist mutant lines. This work was funded by NIH R35GM138203.

## Author contributions

S.J.S.-c. designed the research. H.J.G. and S.J.S.-c. performed experiments. H.J.G., N.C., and S.J.S.-c. analyzed the data. N.C. and S.J.S.-c. developed and N.C. analyzed the physical model. S.D.R. provided optogenetic constructs and valuable support with experimental trouble shooting. H.J.G., N.C., and S.J.S.-c. wrote the initial manuscript. All authors read and contributed to the manuscript. S.J.S.-c. supervised the project.

## Competing interests

The authors declare no competing interests.

## Additional information

**Supplementary information** The online version contains supplementary material available at <https://doi.org/10.1038/s41467-022-34518-9>.

**Correspondence** and requests for materials should be addressed to Nikolas Claussen or Sebastian J. Streichan.

**Peer review information** *Nature Communications* thanks the anonymous reviewers for their contribution to the peer review of this work.

**Reprints and permissions information** is available at <http://www.nature.com/reprints>

**Publisher's note** Springer Nature remains neutral with regard to jurisdictional claims in published maps and institutional affiliations.

**Open Access** This article is licensed under a Creative Commons Attribution 4.0 International License, which permits use, sharing, adaptation, distribution and reproduction in any medium or format, as long as you give appropriate credit to the original author(s) and the source, provide a link to the Creative Commons license, and indicate if changes were made. The images or other third party material in this article are included in the article's Creative Commons license, unless indicated otherwise in a credit line to the material. If material is not included in the article's Creative Commons license and your intended use is not permitted by statutory regulation or exceeds the permitted use, you will need to obtain permission directly from the copyright holder. To view a copy of this license, visit <http://creativecommons.org/licenses/by/4.0/>.

© The Author(s) 2022